

GLEAM: LEARNING TO MATCH AND EXPLAIN IN CROSS-VIEW GEO-LOCALIZATION

Xudong Lu^{1*}, Zhi Zheng^{1*}, Yi Wan², Yongxiang Yao², Annan Wang⁴, Renrui Zhang¹,
 Panwang Xia², Qiong Wu², Qingyun Li⁵, Weifeng Lin¹, Xiangyu Zhao³,
 Peifeng Ma¹, Xue Yang^{3✉}, Hongsheng Li^{1✉}

¹The Chinese University of Hong Kong ²Wuhan University ³Shanghai Jiao Tong University

⁴Nanyang Technological University ⁵Harbin Institute of Technology

*Equal contribution ✉Corresponding author

{luxudong@link, zhizheng, hsli@ee}.cuhk.edu.hk
 yangxue-2019-sjtu@sjtu.edu.cn

ABSTRACT

Cross-View Geo-Localization (CVGL) focuses on identifying correspondences between images captured from distinct perspectives of the same geographical location. However, existing CVGL approaches are typically restricted to a single view or modality, and their direct visual matching strategy lacks interpretability: they only determine whether two images correspond, without explaining the rationale behind the match. In this paper, we present GLEAM-C, a foundational CVGL model that unifies multiple views and modalities—including UAV imagery, street maps, panoramic views, and ground photographs—by aligning them exclusively with satellite imagery. Our framework enhances training efficiency through optimized implementation while achieving accuracy comparable to prior modality-specific CVGL models through a two-phase training strategy. Moreover, to address the lack of interpretability in traditional CVGL methods, we leverage the reasoning capabilities of multimodal large language models (MLLMs) to propose a new task, GLEAM-X, which combines cross-view correspondence prediction with explainable reasoning. To support this task, we construct a bilingual benchmark using GPT-4o and Doubao-1.5-Thinking-Vision-Pro to generate training and testing data. The test set is further refined through detailed human revision, enabling systematic evaluation of explainable cross-view reasoning and advancing transparency and scalability in geo-localization. Together, GLEAM-C and GLEAM-X form a comprehensive CVGL pipeline that integrates multi-modal, multi-view alignment with interpretable correspondence analysis, unifying accurate cross-view matching with explainable reasoning and advancing Geo-Localization by enabling models to better Explain And Match. Code and datasets used in this work will be made publicly accessible at <https://github.com/Lucky-Lance/GLEAM>.

1 INTRODUCTION

Cross-View Geo-Localization (CVGL) seeks to determine the geographic position of a query image by establishing correspondences with a geo-referenced database captured from alternative viewpoints, such as satellite observations. Unlike GNSS, which may suffer from signal blockage or noise in urban canyons and complex environments, CVGL offers a vision-based localization paradigm that is both complementary and robust. This capability has broad relevance to autonomous driving (Cui & Ge, 2003; Chen et al., 2023), robotic navigation (Nowak et al., 2024; Semborski & Idzkowski, 2024), unmanned aerial vehicles (UAVs) navigation (Xu et al., 2024; Suzuki et al., 2016; Wang et al., 2024), and augmented reality devices (Kamalam et al., 2022; Sathyaranayana et al., 2020), where reliable positioning forms the foundation for effective operation.

Despite its practical importance, CVGL remains a technically demanding problem. The task is complicated by the substantial appearance gap across heterogeneous viewpoints and modalities (Regmi & Shah, 2019; Ge et al., 2024). Consequently, prior studies have typically focused on a single

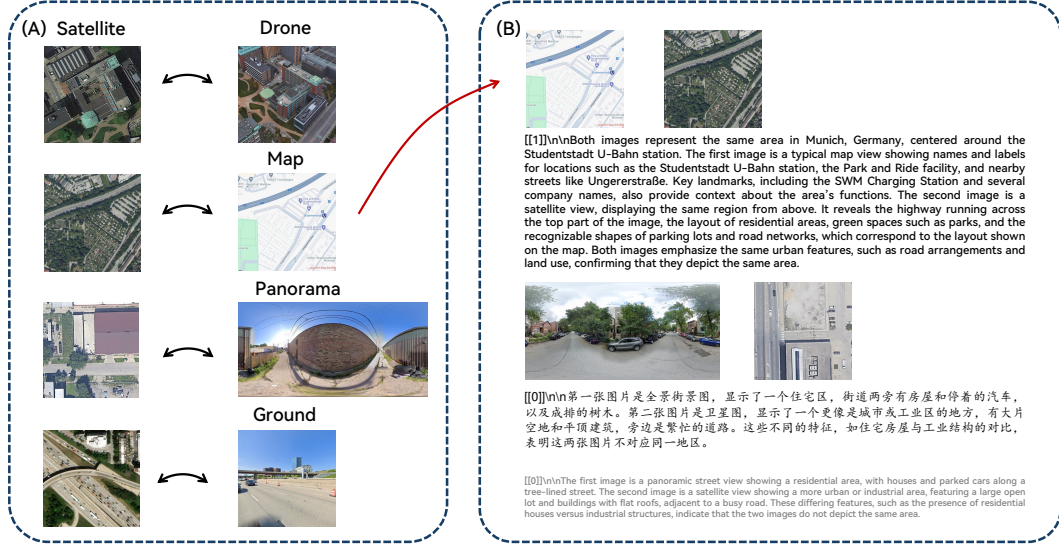


Figure 1: Overview of GLEAM-Core and GLEAM-eXplain. (A) GLEAM-C: a foundational CVGL model trained to align multiple views and modalities—including UAV imagery, street maps, panoramic images, and ground photographs—with satellite imagery. (B) GLEAM-X: a benchmark combining cross-view correspondence prediction with explainable reasoning. We illustrate representative examples of both positive and negative matches between query images and satellite images. The red arrow indicates that GLEAM-C and GLEAM-X can be combined into an integrated pipeline.

viewpoint and modality, such as UAV imagery (Zheng et al., 2020), street maps (Zhao et al., 2021), panoramic views (Zhu et al., 2021), or ground photographs (Wu et al., 2024b). While these modality-specific approaches have achieved promising results, the problem of establishing robust cross-modal alignment within a unified framework remains unresolved. A unified CVGL framework offers several advantages. First, it enables multi-platform deployment through a single inference interface, reducing system complexity, memory footprint, and initialization latency on resource-constrained platforms such as drones and vehicles. Second, it improves robustness and generalization by learning a geographically grounded representation that captures diverse structural regularities. By bridging heterogeneous views and modalities, such a system enables robust, generalizable, and efficient geo-positioning across diverse real-world scenarios.

Moreover, the dominant paradigm in CVGL has been image retrieval or binary correspondence prediction (Deuser et al., 2023a; Xia et al., 2024b), which offers limited interpretability and constrains system transparency. For safety-critical applications such as navigation or disaster response, a mere correspondence score is insufficient; instead, models must provide interpretable reasoning about why two views are matched or mismatched. Recent advances in multimodal large language models (MLLMs) present an avenue for addressing this limitation. By jointly processing visual and textual information, MLLMs can reason about image correspondences and generate human-interpretable explanations (Achiam et al., 2023; Bai et al., 2025a; Zhu et al., 2025). Integrating these reasoning capabilities into CVGL enables models not only to predict whether two images correspond but also to articulate the underlying rationale, enhancing transparency and accountability in decision-making.

To address these two challenges, in this paper, we propose a comprehensive solution that combines robust multi-modal alignment with interpretable cross-view reasoning. The overview of our work is shown in Fig. 1. First, we design GLEAM-Core (GLEAM-C), a foundational CVGL model that integrates multiple views and modalities—including UAV imagery, street maps, panoramic views, and ground photographs—by aligning them exclusively with satellite images. This unified design eliminates the need for modality-specific architectures, thereby simplifying the modeling process and improving scalability across heterogeneous data sources. In GLEAM-C, we reconstruct the conventional Data Parallel (DP) training strategy used in prior work (Deuser et al., 2023b) into a Distributed Data Parallel (DDP) scheme, which yields over 5-fold improvement in training efficiency. We design a two-phase training strategy and evaluate GLEAM-C on both CNN- and ViT-based architectures. The results show accuracy comparable to that of modality-specific models. Second, we design GLEAM-eXplain (GLEAM-X), which combines cross-view correspondence prediction with explainable reasoning. To enhance model robustness, we select 50k query images from the multi-view matching training set, each paired with a positive reference image (match) and a neg-

ative reference image (mismatch). After assigning ground-truth labels, GPT-4o and Doubao-1.5-Thinking-Vision-Pro generate explanations in both Chinese and English, clarifying the reasons for image correspondences. For evaluation, we select 504 query images from the matching test set, each paired with a positive and a negative reference image. After GPT-4o generates explanations, we perform multiple rounds of human annotation and refinement to create a high-quality test set. We fine-tune the Qwen2.5-VL-3B-Instruct MLLM on the training set, achieving higher matching accuracy than GPT-4o and Doubao-1.5, with analysis results closely aligned with human annotations. GLEAM-C and GLEAM-X can be further integrated: GLEAM-C performs the core task of cross-view geo-localization by aligning query images with geo-referenced satellite imagery. GLEAM-X enhances this process by verifying and providing human-interpretable explanations for the image correspondences predicted by GLEAM-C, improving both the model’s robustness and transparency. The contributions of our work can be summarized as follows:

- 1) Problem Analysis:** We provide a detailed analysis of the CVGL task, highlight the benefits of a unified CVGL framework, and identify the lack of interpretability in current CVGL solutions.
- 2) GLEAM-C:** We propose GLEAM-C, a foundational CVGL model that unifies multiple views and modalities—including UAV images, street maps, panoramic images, and ground photographs—by aligning them with satellite images. We adopt a two-phase training strategy and leverage DDP to optimize training efficiency, achieving accuracy comparable to modality-specific CVGL models.
- 3) GLEAM-X:** We introduce the GLEAM-X benchmark, combining cross-view correspondence prediction with explainable reasoning. We provide a high-quality bilingual (Chinese-English) training and testing dataset, along with the Qwen2.5-VL-3B-Instruct model fine-tuned on this dataset. This enables the generation of human-interpretable explanations for image correspondences, thereby enhancing the robustness and transparency of the model.
- 4) Integrated Pipeline:** GLEAM-C and GLEAM-X can be combined into an integrated pipeline. GLEAM-C performs the core task of CVGL by aligning query images with satellite imagery, while GLEAM-X enhances this process by verifying and providing human-interpretable explanations for the predicted correspondences, improving both the model’s robustness and transparency.

2 RELATED WORKS

2.1 CROSS-VIEW GEO-LOCALIZATION

Cross-View Geo-Localization (CVGL) has garnered substantial attention within the research community. Most existing research, however, focuses on a single view or modality. Early efforts construct paired ground-to-aerial datasets (Lin et al., 2015), which later evolve into widely used benchmarks such as CVUSA (Workman et al., 2015), CVACT (Liu & Li, 2019), VIGOR (Zhu et al., 2021), University-1652 (Zheng et al., 2020), and DenseUAV (Dai et al., 2023), enabling evaluations across panoramas, UAV imagery, and related scenarios. Methodologically, handcrafted descriptors (Bansal et al., 2011; Castaldo et al., 2015) soon give way to deep learning, where pre-trained CNNs and fine-tuning strategies significantly advance cross-view correspondence (Krizhevsky et al., 2012; Workman et al., 2015). Subsequent studies introduce a variety of techniques to alleviate viewpoint discrepancies, including polar and optimal transport transformations (Shi et al., 2020; 2019), region-level and latent alignment (Dai et al., 2021; Xia et al., 2024a), and strategies that enhance scene discrimination, such as hard-negative mining (Deuser et al., 2023b) and cross-dimension interactions (Shen et al., 2023). More recently, unsupervised approaches explore how to exploit unlabeled data for training (Li et al., 2024c;b). Despite these advancements, most studies remain modality-specific, and the development of a unified framework that accommodates diverse modalities still represents an open challenge.

2.2 MULTIMODAL LARGE LANGUAGE MODEL

Multimodal large language models (MLLMs) have emerged in recent years as a powerful tool for handling complex tasks by incorporating visual inputs into traditional language models (OpenAI, 2023; Liu et al., 2024; Chen et al., 2024; Bai et al., 2025a). Prominent commercial models such as OpenAI’s GPT-4o (Hurst et al., 2024) and Google’s Gemini 2.5 (Comanici et al., 2025) exemplify this trend by simultaneously handling text, audio, images, and video, unlocking new capabilities like

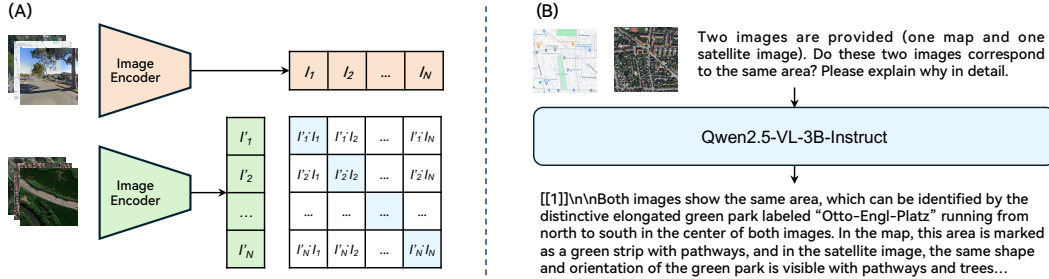


Figure 2: Method Overview of GLEAM-C and GLEAM-X. (A) GLEAM-C: We apply a contrastive learning architecture to train the CVGL model across UAV, street map, panoramic, and ground photographs. (B) GLEAM-X: This component formulates a multi-image reasoning task. The MLLM receives a query image, a reference image, and a natural language instruction. Through fine-tuning, it delivers both a matching prediction and an interpretable textual explanation.

Dataset	Original Pairs	GLEAM-C		GLEAM-X	
		Sampling Ratio	Training Pairs	Sampling Ratio	Training Pairs (pos+neg, en+zh)
University-1652 (Zheng et al., 2020)	37,854	1.00	37,854	0.36	54,000
VIGOR (Zhu et al., 2021)	52,609	1.00	52,609	0.26	54,000
SetVL-480K (Wu et al., 2024a)	240,544	0.50	120,272	0.06	54,000
MAP	10,208	4.00	40,832	1.00	40,832
Total	341,215	—	251,567	—	202,832

Table 1: Statistics of training pairs in GLEAM-C and GLEAM-X. GLEAM-C primarily constructs training pairs from existing CVGL datasets. GLEAM-X balances the data distribution across datasets and then samples positive and negative pairs, providing bilingual explanation annotations.

real-time, human-like voice interaction and long-context video understanding. In addition to closed-source commercial MLLMs, numerous well-known open-source models, such as InternVL3 (Wang et al., 2025), Qwen2.5-VL (Bai et al., 2025b), MiniCPM-V 4.5 (Yao et al., 2024), and LLaVA-OneVision (Li et al., 2024a), have made significant contributions to advancing multimodal understanding. Beyond perception alone, recent efforts increasingly emphasize unifying multimodal understanding and generation, thereby enabling models not only to interpret visual inputs but also to synthesize new content. Representative examples include Janus-Pro (Chen et al., 2025), Show-o (Xie et al., 2024), and BAGEL (Deng et al., 2025), which collectively mark a transition toward more general-purpose multimodal intelligence that integrates both reasoning and creativity.

3 GLEAM-C: A UNIFIED CVGL CORE MODEL

GLEAM-C is designed as a unified CVGL model, leveraging a contrastive learning paradigm to align visual representations across diverse viewpoints and modalities. In this section, we provide the data composition (Sec. 3.1), model structure (Sec. 3.2), and training recipe (Sec. 3.3).

3.1 DATA COMPOSITION

GLEAM-C is a foundational CVGL model that aligns multiple views and modalities—including UAV imagery, street maps, panoramic views, and ground photographs—exclusively with satellite imagery. To facilitate training, we utilize widely adopted datasets from prior work: University-1652 (Zheng et al., 2020) for UAV imagery, VIGOR (Zhu et al., 2021) for panoramic views, and SetVL-480K (Wu et al., 2024a) for ground photographs. In addition, for street maps, we manually collect 12,761 pairs of corresponding street maps and satellite images from Google Maps, with each image resized to 512×512 pixels. We use 10,208 pairs for training and 2,553 pairs for testing.

The original datasets show highly imbalanced sample distributions across different views and modalities, as shown in Tab. 1, which could introduce biases and hinder the model from learning uniformly. To mitigate this issue, we employ data sampling to balance the number of samples across all views and modalities. This ensures that the model receives sufficient and diverse training signals from each type of data, thereby improving its robustness across heterogeneous inputs. For evaluation, we adhere to the original test datasets and protocols provided by each benchmark. The newly introduced MAP test follows the same evaluation logic as VIGOR (Zhu et al., 2021).

3.2 MODEL STRUCTURE

We leverage a contrastive training strategy for GLEAM-C, where the query and reference images share the same encoder for feature extraction. The InfoNCE loss is applied to learn discriminative features across both view directions. The training framework is shown in Fig. 2A. Our implementation is based on the well-engineered Sample4Geo (Deuser et al., 2023b) codebase. Notably, Sample4Geo introduces GPS-Sampling (GPS) and Dynamic Similarity Sampling (DSS) to select hard negatives during training, thereby improving optimization efficiency. However, certain datasets, such as University-1652 (Zheng et al., 2020), do not provide GPS metadata. Therefore, GLEAM-C relies solely on DSS. In our experiments, we evaluate both convolutional and transformer-based architectures as backbones. Specifically, we adopt ConvNeXt (Liu et al., 2022), comprising 88.6M parameters, and the Perception Encoder (Bolya et al., 2025), comprising 0.32B parameters.

3.3 TRAINING RECIPE

We propose a two-phase training scheme to effectively integrate knowledge across multiple modalities and views (Sec. 3.3.1). Given the substantial data requirements of foundational model training and the limited efficiency of the original Sample4Geo codebase, we implement targeted optimizations to significantly enhance training efficiency (Sec. 3.3.2).

3.3.1 TWO-PHASE TRAINING STRATEGY

We note that a naive concatenation of multiple datasets for training from the outset poses significant challenges. Due to the backbone model’s limited matching capacity and the varying dataset sizes and difficulty levels, direct multi-dataset training often results in highly imbalanced performance. To mitigate this issue, we first train the model on a single dataset that is relatively large and of moderate difficulty, allowing the backbone to acquire fundamental CVGL capabilities before introducing more complex and diverse data. In our design, we first train the model on the VIGOR (Zhu et al., 2021) dataset for 40 epochs, followed by training on the concatenated datasets for an additional 40 epochs.

3.3.2 TRAINING EFFICIENCY IMPROVEMENT

Similar to CLIP training, contrastive learning models typically require large batch sizes. The original Sample4Geo adopts PyTorch’s Data Parallel (DP) strategy, where GPU 0 distributes data, aggregates outputs, and performs gradient updates for the entire cluster. This centralized design creates a significant communication bottleneck on GPU 0, thus slowing the training process. Distributed Data Parallel (DDP) alleviates this issue by allowing each GPU to compute gradients locally and synchronizing them via an efficient all-reduce. However, contrastive learning relies on in-batch negatives, and small per-GPU batch sizes limit the number of negatives available per device, potentially degrading performance. This underscores the importance of maintaining sufficiently large per-GPU batch sizes even when using DDP. To tackle this issue, we adopt the strategy implemented in Open-CLIP (Ilharco et al., 2021). Before computing the contrastive loss, each GPU (rank) gathers the feature representations from all other GPUs. These features are then re-concatenated, effectively creating a unified global batch for the loss calculation on each device. This process preserves the gradient flow for proper backpropagation while providing every GPU with a much larger and more effective set of negative samples. For clarity, we provide pseudocode for the loss computation in Alg. 1 in Sec. A.1. This implementation achieves over 5-fold faster training speed while maintaining the original model accuracy.

4 GLEAM-X: A MULTI-IMAGE MLLM EXPLANATION BENCHMARK

GLEAM-X extends GLEAM-C to a multi-image reasoning setting, where the model not only predicts matches between query and reference images but also generates interpretable explanations. **In practice, GLEAM-C and GLEAM-X operate as an integrated pipeline:** GLEAM-C first retrieves the best-matching reference image for a given query, and GLEAM-X then verifies whether this reference image truly matches the query while providing human-interpretable explanations. In this section, we present the data composition (Sec. 4.1), annotation procedure (Sec. 4.2), and evaluation protocol (Sec. 4.3) of the GLEAM-X benchmark.

4.1 DATA COMPOSITION

Our training and testing data pairs are derived from the GLEAM-C training and test sets. To maintain balance across modalities and views, we perform data sampling to ensure that the amount of training data for each modality is roughly equal, as shown in Tab. 1. In the evaluation of GLEAM-X, we also maintain this balance across modalities. The selected query images for testing include 128 for MAP, 126 for SetVL-480K, 127 for University-1652, and 123 for VIGOR. For each query image, we select one positive reference image and one negative reference image. Using the corresponding labels, we generate explanation annotations in both English and Chinese with commercial MLLMs, specifically GPT-4o (Hurst et al., 2024) and Doubao-1.5-Thinking-Vision-Pro (Volcengine, 2025).

During explanation construction, the commercial MLLMs are provided with ground-truth labels indicating whether a given query-reference pair matches, guiding them to generate explanations accordingly. This introduces explicit prior knowledge, thereby enhancing the correctness of the generated responses. During MLLM training, the ground-truth label is concatenated with the explanations produced by the commercial MLLMs and used as the target output. For example, for a positive sample pair, the model is trained to produce the response `[[1]]\n\n(explanation)`. Such a format enables straightforward extraction of match labels, supporting both training supervision and evaluation of matching performance. Using this approach, we construct 200k training pairs with GPT-4o and Doubao-1.5-Thinking-Vision-Pro, respectively, and 2k test pairs with GPT-4o. The architecture employed for MLLM training and inference is shown in Fig. 2B.

4.2 DATA ANNOTATION

To ensure the accuracy of the test set, we manually revise the 2k test pairs. We engage 4 human experts in Remote Sensing, each holding at least a master’s degree, to perform data annotation and revision. We conduct two annotation rounds: in each round, we first verify the correctness of the explanations generated by the commercial MLLMs and correct them if necessary; if the four experts cannot determine whether a query and reference image match, we replace the pair with a suitable one from the remaining test data and perform model-assisted generation followed by manual correction. This ensures that all test pairs are valid and unambiguous, providing a reliable basis for evaluation.

4.3 EVALUATION PROTOCOL

We evaluate the MLLM outputs on the test set from two perspectives. First, we extract the predicted match labels using regular-expression parsing and compute the matching accuracy. Second, we assess the quality of the generated explanations by measuring their semantic similarity to the annotated references with Sentence-BERT (Reimers & Gurevych, 2019). This dual evaluation framework ensures a comprehensive assessment, as it captures both the correctness of structured match predictions and the semantic fidelity of explanatory outputs.

5 EXPERIMENTS

In this section, we design a series of experiments to evaluate the unified GLEAM-C model (Sec. 5.1) and the GLEAM-X benchmark (Sec. 5.2). All training experiments are conducted on a cluster equipped with 10 NVIDIA RTX 4090 D GPUs, each with 48 GB of memory.

5.1 EVALUATION RESULTS OF GLEAM-C

For GLEAM-C, we compare the unified model with single-dataset training and evaluate the data integration strategy (Sec.5.1.1). We further assess improvements in training efficiency (Sec.5.1.2) relative to prior SOTA training methods.

5.1.1 FROM SINGLE DATASET TO MULTI-DATASET INTEGRATION

As in most CVGL studies, we first train on single-view and single-modality datasets. Training is conducted separately on the VIGOR (same), University-1652, MAP, and SetVL-480K ($N = 1$) datasets. Model performance is evaluated using image retrieval accuracy, with University-1652 following the

Backbone	Training Strategy	Dataset	Epochs	R@1	R@5	R@10	Top-1	AP/HR
ConvNeXt-B-384	Single-dataset	[†] VIGOR	40	77.86	95.66	97.21	99.61	89.82
	Sample4Geo	University-1652	1	92.65	-	-	-	93.81
	[†] GPS + DSS	[†] SetVL-480K	40	16.86	38.95	47.71	85.40	16.86
ConvNeXt-B-384	Single-dataset	VIGOR	40	76.60	95.07	96.83	99.64	88.29
	Sample4Geo	University-1652	1	91.55	97.79	98.37	98.44	92.98
	w/o GPS	MAP	40	92.60	98.08	98.94	99.80	92.60
		SetVL-480K	40	14.23	34.10	44.63	71.67	14.23
ConvNeXt-B-384	From-scratch (Merge)	VIGOR		73.37	93.43	95.66	99.61	84.43
		University-1652	40	87.08	95.22	96.59	96.79	88.96
		MAP		92.52	97.81	98.79	99.80	92.52
		SetVL-480K		14.33	34.30	44.77	70.75	14.33
PE-Core-L14-336	Two-phase (VIGOR → Merge)	VIGOR		75.66	94.51	96.43	99.65	86.80
		University-1652	40	87.03	96.11	97.84	98.03	89.12
		MAP		94.05	98.04	98.71	99.65	94.05
		SetVL-480K		15.28	35.49	45.71	71.30	15.28
PE-Core-L14-336	Single-dataset	VIGOR	40	75.53	95.48	97.18	99.67	89.46
		University-1652	1	94.38	98.44	98.80	98.85	95.32
		MAP	40	92.79	97.92	98.55	99.73	92.79
		SetVL-480K	40	21.34	46.54	57.95	81.58	21.34
PE-Core-L14-336	From-scratch (Merge)	VIGOR		69.44	92.81	95.43	99.63	83.18
		University-1652	40	93.20	97.73	98.30	98.40	94.26
		MAP		93.11	98.32	98.75	99.73	93.11
		SetVL-480K		22.00	46.93	58.28	81.83	22.00
PE-Core-L14-336	Two-phase (VIGOR → Merge)	VIGOR		75.96	95.46	97.17	99.68	89.44
		University-1652	40	93.19	97.92	98.49	98.57	94.28
		MAP		93.97	98.20	98.43	99.77	93.97
		SetVL-480K		23.25	48.61	59.76	82.98	23.25

Table 2: Image retrieval accuracy across backbones and training strategies. For University-1652, the last evaluation metric is AP; for all other datasets, it is Hit Rate. The first three rows (highlighted in gray) are directly taken from the corresponding papers with GPS (if applicable, marked with [†]) and DSS sampling for reference. It can be observed that using a two-phase training strategy yields relatively stronger performance. The unified GLEAM-C model achieves results comparable to or even exceeding those obtained by single-dataset training (Sample4Geo w/o GPS-Sampling).

Dataset	Mode	Recall@1	Recall@5	Recall@10	Recall@top1	Hit Rate	Seconds/Epoch
VIGOR	DP	76.80	95.06	96.70	99.25	89.05	521
	DDP	76.60	95.07	96.83	99.64	88.29	92

Table 3: Image retrieval accuracy comparison between Data Parallel (DP) and Distributed Data Parallel (DDP) on the VIGOR dataset with ConvNeXt-B backbone using Sample4Geo codebase. Both approaches achieve comparable accuracy, while DDP attains over 5× faster training speed.

Drone2Sat protocol. We adopt ConvNeXt-B-384 (88.6M) and PE-Core-L14-336 (0.32B) as the image encoders. The results for single-dataset training are presented in Tab. 2. Since some datasets lack GPS metadata, we do not use GPS sampling in all our model training, which may result in a slight decrease in accuracy. For reference, we also report the original metrics from the respective papers, with GPS (if applicable) and DSS sampling (Deuser et al., 2023b; Wu et al., 2024a).

To train the unified model, we compare two data integration strategies in our work. The first strategy trains on mixed data directly from the backbone’s initial weights, while the second strategy starts training from a VIGOR checkpoint obtained through single-dataset training. We use the data sampling ratios shown in Tab. 1, and both strategies are trained for 40 epochs. We provide the results in Tab. 2 and share the following observations:

1) Directly training on the mixed data degrades the performance on VIGOR. However, continuing training the unified model from a VIGOR checkpoint yields better results and improves accuracy on MAP and SetVL-480K. This highlights the importance of endowing the model with basic CVGL capability before performing mixed-data training, and also suggests that learning across different views and modalities may mutually reinforce each other.

Model	Language	MAP	SetVL-480K	University-1652	VIGOR	Avg Acc
GPT-4o		85.55	63.89	93.70	81.71	81.25
Doubao-1.5		91.80	74.21	60.24	83.74	77.48
Qwen2.5-VL-3B-Instruct +label only +GPT-4o +Doubao-1.5	EN	55.08	57.94	51.57	65.04	57.34
		96.88	84.13	97.64	92.28	92.76
		94.53	78.17	99.61	89.02	90.38
		95.31	79.37	96.46	87.80	89.78
Model	Language	MAP	SetVL-480K	University-1652	VIGOR	Avg Acc
GPT-4o		85.55	70.63	96.06	82.11	83.63
Doubao-1.5		89.45	78.97	66.93	81.30	79.17
Qwen2.5-VL-3B-Instruct +label only +GPT-4o +Doubao-1.5	ZH	51.17	51.19	50.00	49.59	50.50
		96.88	84.13	97.64	92.28	92.76
		95.31	76.59	99.61	89.02	90.18
		94.53	75.00	94.88	86.59	87.80

Table 4: Matching accuracy comparison of different models on GLEAM-X in English and Chinese. Results are reported on MAP, SetVL-480K, University-1652, and VIGOR datasets, along with the overall average accuracy. Label-only supervision and LLM-explanation supervision (+GPT-4o, +Doubao-1.5) significantly improve the performance of Qwen2.5-VL-3B-Instruct.

Model	Language	0.0-0.2	0.2-0.4	0.4-0.6	0.6-0.8	0.8-1.0	Avg Sim
GPT-4o		0.0%	0.1%	0.8%	21.6%	77.5%	0.8349
Doubao-1.5		0.0%	0.0%	0.2%	33.5%	66.3%	0.8171
Qwen2.5-VL-3B-Instruct +label only +GPT-4o +Doubao-1.5	EN	0.8%	0.0%	2.0%	59.3%	37.9%	0.7645
		99.9%	0.1%	0.0%	0.0%	0.0%	0.0981
		0.0%	0.0%	0.1%	22.4%	77.5%	0.8405
		0.0%	0.0%	0.5%	36.0%	63.5%	0.8122
Model	Language	0.0-0.2	0.2-0.4	0.4-0.6	0.6-0.8	0.8-1.0	Avg Sim
GPT-4o		1.6%	5.0%	2.3%	50.5%	40.7%	0.7403
Doubao-1.5		0.0%	0.0%	4.5%	66.7%	28.9%	0.7495
Qwen2.5-VL-3B-Instruct +label only +GPT-4o +Doubao-1.5	ZH	4.2%	0.1%	2.9%	58.5%	34.3%	0.7399
		92.1%	7.9%	0.0%	0.0%	0.0%	0.1476
		0.0%	0.0%	0.3%	32.5%	67.2%	0.8239
		0.4%	0.0%	1.1%	46.6%	51.9%	0.7924

Table 5: Similarity score distribution (by Sentence-BERT) for different models on GLEAM-X in English and Chinese. Columns show percentages in each similarity range (0.0–0.2, ..., 0.8–1.0) and the last column reports Avg Sim. LLM-explanation supervision (+GPT-4o, +Doubao-1.5) improves alignment with ground-truth, while label-only supervision fails to generate explanations.

- 2) Compared with single-dataset training, our two-phase training strategy yields the foundational GLEAM-C model, which attains comparable or superior performance across all evaluated datasets.
- 3) The larger PE-Core-L14-336 model achieves overall better performance compared to ConvNeXt-B-384 after training. Additionally, although University-1652 requires only a single epoch of training, we train for 40 epochs due to the demands of mixed-data training; under this setting, smaller models may suffer from overtraining or instability, whereas larger models remain largely unaffected.

5.1.2 TRAINING EFFICIENCY EVALUATION

We evaluate training efficiency on the VIGOR dataset by comparing DP and DDP strategies. Following the experiment settings of Sample4Geo (Deuser et al., 2023b), we adopt the ConvNeXt-B-384 backbone and use the original Sample4Geo code for DP training (without GPS-based sampling). As shown in Tab. 3, both approaches achieve comparable image retrieval accuracy across all Recall@k and Hit Rate metrics. However, DDP demonstrates a substantial (5-fold) speed advantage, reducing the time per training epoch from 521 seconds to 92 seconds, highlighting its effectiveness for accelerating large-scale CVGL model training.

5.2 EVALUATION RESULTS ON GLEAM-X

We evaluate both commercial models and open-source models on the GLEAM-X benchmark. For commercial models, we regenerate answers on the test set using GPT-4o and Doubao-1.5-

Model	Language	Pos Acc	Neg Acc	Pos-Neg	Pos Sim	Neg Sim	Pos-Neg
GPT-4o		70.83	91.67	-20.84	0.8296	0.8401	-0.0105
Doubao-1.5		66.87	88.10	-21.23	0.8100	0.8241	-0.0141
Qwen2.5-VL-3B-Instruct +label only +GPT-4o +Doubao-1.5	EN	23.81	90.87	-67.06	0.7616	0.7675	-0.0059
		93.85	91.67	2.18	0.0851	0.1111	-0.0260
		93.25	87.50	5.75	0.8399	0.8411	-0.0012
		90.08	89.48	0.60	0.8048	0.8195	-0.0147
Model	Language	Pos Acc	Neg Acc	Pos-Neg	Pos Sim	Neg Sim	Pos-Neg
GPT-4o		73.02	94.25	-21.23	0.7337	0.7468	-0.0131
Doubao-1.5		76.19	82.14	-5.95	0.7435	0.7555	-0.0120
Qwen2.5-VL-3B-Instruct +label only +GPT-4o +Doubao-1.5	ZH	1.19	99.80	-98.61	0.7265	0.7533	-0.0268
		93.85	91.67	2.18	0.1471	0.1481	-0.0010
		90.87	89.48	1.39	0.8211	0.8267	-0.0056
		84.52	91.07	-6.55	0.7858	0.7989	-0.0131

Table 6: Positive and negative sample accuracy (Pos/Neg Acc) and similarity (Pos/Neg Sim) for different models on GLEAM-X in English and Chinese. The Pos-Neg columns report the difference between positive and negative samples. Vanilla Qwen2.5-VL-3B-Instruct shows a strong bias toward predicting non-matching pairs, while LLM-explanation supervision (+GPT-4o, +Doubao-1.5) mitigates this bias and improves alignment with ground-truth explanations.

Thinking-Vision-Pro without providing ground-truth labels. For open-source models, we compare three variants of Qwen2.5-VL-3B-Instruct: the original model, the version fine-tuned with LLM-explanation supervision, and a version trained solely with label-only supervision. Specifically, for the explanation-based variant, we follow the procedure in Sec. 4.1, concatenating labels and explanations during training. We train separately on the 200k explanations generated by GPT-4o and Doubao-1.5 for 1 epoch. Conversely, the label-only variant uses only labels (e.g., [[1]]) for training.

After inference on the test set, we decouple matching predictions and explanations through regularization to isolate their respective contributions. To provide a comprehensive evaluation of GLEAM-X, we perform detailed analyses from three perspectives: matching accuracy (Sec.5.2.1), semantic accuracy (Sec.5.2.2), and positive/negative sample analysis (Sec. 5.2.3).

5.2.1 MATCHING ACCURACY

The matching accuracy results are presented in Tab. 4. Commercial models achieve a relatively strong performance of around 80%, with GPT-4o outperforming Doubao-1.5 on average. In contrast, the original Qwen2.5-VL-3B-Instruct model exhibits very low accuracy, particularly in the Chinese setting, where its accuracy is only 50.50%. After training, all model variants obtain accuracy surpassing that of the commercial MLLMs. Notably, the label-only supervision model achieves the highest accuracy, likely because its training targets are extremely short (e.g., [[0]] or [[1]]), which reduces the learning difficulty for the model.

5.2.2 SEMANTIC ANALYSIS OF EXPLANATIONS

Tab. 5 reveals the similarity distributional differences across models. Commercial MLLMs concentrate heavily in the high-similarity range (0.8–1.0) for English, but shift toward 0.6–0.8 in Chinese. The original Qwen2.5-VL-3B-Instruct places a substantial proportion of predictions in the mid-similarity bins (0.6–0.8) for both languages, indicating weaker semantic alignment with ground-truth explanations. Fine-tuning with LLM-explanation supervision shifts the distribution upward, with both +GPT-4o and +Doubao-1.5 variants peaking in the 0.8–1.0 range. By contrast, the label-only supervision model collapses almost entirely into the lowest bin (0.0–0.2), confirming its inability to generate semantically meaningful explanations despite improvements in matching accuracy.

5.2.3 ANALYSIS OF POSITIVE AND NEGATIVE PAIR SAMPLES

To further analyze model behavior on positive and negative samples, we examine both matching accuracy and semantic similarity in Tab. 6. Vanilla MLLMs, including both commercial models and Qwen2.5-VL-3B-Instruct, exhibit a bias toward negative samples. In particular, Qwen2.5-VL-3B-Instruct achieves very low positive accuracy while maintaining high negative accuracy, indicating that the original model tends to predict image pairs as non-matching. Fine-tuning with LLM-explanation supervision (+GPT-4o, +Doubao-1.5) substantially mitigates this bias, raising

positive accuracy to over 90% in English and over 84% in Chinese, while still keeping negative accuracy high. Correspondingly, positive and negative similarity are more balanced. Overall, LLM-explanation supervision effectively improves both prediction balance and explanation quality across languages. In contrast, the label-only supervision variant achieves high positive accuracy but fails to generate semantically meaningful explanations, as evidenced by extremely low similarity scores.

6 CONCLUSION

In this paper, we systematically address the challenges of cross-view geo-localization by making several key contributions. First, we provide a detailed analysis of the CVGL problem, highlighting the benefits of a unified framework for integrating multiple views and modalities, and emphasizing the importance of interpretability and system transparency in practical applications. Second, we propose GLEAM-C, a foundational model that aligns diverse viewpoints and modalities with satellite imagery, improving training efficiency and achieving high accuracy through a two-phase training strategy. Third, we introduce GLEAM-X, a bilingual benchmark that enables explainable reasoning, allowing the generation of human-interpretable explanations for image correspondences and enhancing model transparency. GLEAM-C and GLEAM-X can be integrated into a unified pipeline that combines accurate correspondence prediction with interpretable explanations, improving both robustness and trustworthiness of CVGL systems. We hope that our work will contribute to advancing research and development in this field of study.

REFERENCES

Josh Achiam, Steven Adler, Sandhini Agarwal, Lama Ahmad, Ilge Akkaya, Florencia Leoni Aleman, Diogo Almeida, Janko Altenschmidt, Sam Altman, Shyamal Anadkat, et al. GPT-4 technical report. *arXiv preprint arXiv:2303.08774*, 2023.

Shuai Bai, Keqin Chen, Xuejing Liu, Jialin Wang, Wenbin Ge, Sibo Song, Kai Dang, Peng Wang, Shijie Wang, Jun Tang, Humen Zhong, Yuanzhi Zhu, Mingkun Yang, Zhaohai Li, Jianqiang Wan, Pengfei Wang, Wei Ding, Zheren Fu, Yiheng Xu, Jiabo Ye, Xi Zhang, Tianbao Xie, Zesen Cheng, Hang Zhang, Zhibo Yang, Haiyang Xu, and Junyang Lin. Qwen2.5-vl technical report. *ArXiv*, abs/2502.13923, 2025a. URL <https://api.semanticscholar.org/CorpusID:276449796>.

Shuai Bai, Keqin Chen, Xuejing Liu, Jialin Wang, Wenbin Ge, Sibo Song, Kai Dang, Peng Wang, Shijie Wang, Jun Tang, et al. Qwen2.5-vl technical report. *arXiv preprint arXiv:2502.13923*, 2025b.

Mayank Bansal, Harpreet S Sawhney, Hui Cheng, and Kostas Daniilidis. Geo-localization of street views with aerial image databases. In *Proceedings of the 19th ACM international conference on Multimedia*, pp. 1125–1128, 2011.

Daniel Bolya, Po-Yao Huang, Peize Sun, Jang Hyun Cho, Andrea Madotto, Chen Wei, Tengyu Ma, Jiale Zhi, Jathushan Rajasegaran, Hanoona Rasheed, Junke Wang, Marco Monteiro, Hu Xu, Shiyu Dong, Nikhila Ravi, Daniel Li, Piotr Dollár, and Christoph Feichtenhofer. Perception encoder: The best visual embeddings are not at the output of the network. *arXiv:2504.13181*, 2025.

Francesco Castaldo, Amir Zamir, Roland Angst, Francesco Palmieri, and Silvio Savarese. Semantic cross-view matching. In *Proceedings of the IEEE International Conference on Computer Vision Workshops*, pp. 9–17, 2015.

Liang Chen, Fu Zheng, Xiaopeng Gong, and Xinyuan Jiang. Gnss high-precision augmentation for autonomous vehicles: Requirements, solution, and technical challenges. *Remote Sensing*, 15(6):1623, 2023.

Xiaokang Chen, Zhiyu Wu, Xingchao Liu, Zizheng Pan, Wen Liu, Zhenda Xie, Xingkai Yu, and Chong Ruan. Janus-pro: Unified multimodal understanding and generation with data and model scaling. *arXiv preprint arXiv:2501.17811*, 2025.

Zhe Chen, Jiannan Wu, Wenhai Wang, Weijie Su, Guo Chen, Sen Xing, Muyan Zhong, Qinglong Zhang, Xizhou Zhu, Lewei Lu, et al. Internvl: Scaling up vision foundation models and aligning for generic visual-linguistic tasks. In *Proceedings of the IEEE/CVF Conference on Computer Vision and Pattern Recognition*, pp. 24185–24198, 2024.

Gheorghe Comanici, Eric Bieber, Mike Schaeckermann, Ice Pasupat, Noveen Sachdeva, Inderjit Dhillon, Marcel Blstein, Ori Ram, Dan Zhang, Evan Rosen, et al. Gemini 2.5: Pushing the frontier with advanced reasoning, multimodality, long context, and next generation agentic capabilities. *arXiv preprint arXiv:2507.06261*, 2025.

Youjing Cui and Shuzhi Sam Ge. Autonomous vehicle positioning with gps in urban canyon environments. *IEEE transactions on robotics and automation*, 19(1):15–25, 2003.

Ming Dai, Jianhong Hu, Jiedong Zhuang, and Enhui Zheng. A transformer-based feature segmentation and region alignment method for uav-view geo-localization. *IEEE Transactions on Circuits and Systems for Video Technology*, 32(7):4376–4389, 2021.

Ming Dai, Enhui Zheng, Zhenhua Feng, Lei Qi, Jiedong Zhuang, and Wankou Yang. Vision-based uav self-positioning in low-altitude urban environments. *IEEE Transactions on Image Processing*, 33:493–508, 2023.

Chaorui Deng, Deyao Zhu, Kunchang Li, Chenhui Gou, Feng Li, Zeyu Wang, Shu Zhong, Weihao Yu, Xiaonan Nie, Ziang Song, Guang Shi, and Haoqi Fan. Emerging properties in unified multimodal pretraining. *arXiv preprint arXiv:2505.14683*, 2025.

Fabian Deuser, Konrad Habel, and Norbert Oswald. Sample4geo: Hard negative sampling for cross-view geo-localisation. *2023 IEEE/CVF International Conference on Computer Vision (ICCV)*, pp. 16801–16810, 2023a. URL <https://api.semanticscholar.org/CorpusID:257636648>.

Fabian Deuser, Konrad Habel, and Norbert Oswald. Sample4geo: Hard negative sampling for cross-view geo-localisation. In *Proceedings of the IEEE/CVF International Conference on Computer Vision*, pp. 16847–16856, 2023b.

Fawei Ge, Yunzhou Zhang, Yixiu Liu, Guiyuan Wang, Sonya A. Coleman, D. Kerr, and Li Wang. Multibranch joint representation learning based on information fusion strategy for cross-view geo-localization. *IEEE Transactions on Geoscience and Remote Sensing*, 62:1–16, 2024. URL <https://api.semanticscholar.org/CorpusID:268594513>.

Aaron Hurst, Adam Lerer, Adam P Goucher, Adam Perelman, Aditya Ramesh, Aidan Clark, AJ Osztrow, Akila Welihinda, Alan Hayes, Alec Radford, et al. Gpt-4o system card. *arXiv preprint arXiv:2410.21276*, 2024.

Gabriel Ilharco, Mitchell Wortsman, Ross Wightman, Cade Gordon, Nicholas Carlini, Rohan Taori, Achal Dave, Vaishaal Shankar, Hongseok Namkoong, John Miller, Hannaneh Hajishirzi, Ali Farhadi, and Ludwig Schmidt. Openclip, July 2021. URL <https://doi.org/10.5281/zenodo.5143773>. If you use this software, please cite it as below.

GK Kamalam, Shubham Joshi, Manish Maheshwari, K Senthamil Selvan, Sajjad Shaukat Jamal, S Vairaprakash, and Musah Alhassan. Augmented reality-centered position navigation for wearable devices with machine learning techniques. *Journal of Healthcare Engineering*, 2022(1):1083978, 2022.

Alex Krizhevsky, Ilya Sutskever, and Geoffrey E Hinton. Imagenet classification with deep convolutional neural networks. *Advances in neural information processing systems*, 25, 2012.

Bo Li, Yuanhan Zhang, Dong Guo, Renrui Zhang, Feng Li, Hao Zhang, Kaichen Zhang, Yanwei Li, Ziwei Liu, and Chunyuan Li. Llava-onevision: Easy visual task transfer. *arXiv preprint arXiv:2408.03326*, 2024a.

Guopeng Li, Ming Qian, and Gui-Song Xia. Unleashing unlabeled data: A paradigm for cross-view geo-localization. In *Proceedings of the IEEE/CVF Conference on Computer Vision and Pattern Recognition*, pp. 16719–16729, 2024b.

Haoyuan Li, Chang Xu, Wen Yang, Huai Yu, and Gui-Song Xia. Learning cross-view visual geo-localization without ground truth. *IEEE Transactions on Geoscience and Remote Sensing*, 2024c.

Tsung-Yi Lin, Yin Cui, Serge Belongie, and James Hays. Learning deep representations for ground-to-aerial geolocalization. In *Proceedings of the IEEE conference on computer vision and pattern recognition*, pp. 5007–5015, 2015.

Haotian Liu, Chunyuan Li, Qingyang Wu, and Yong Jae Lee. Visual instruction tuning. *NeurIPS*, 36, 2024.

Liu Liu and Hongdong Li. Lending orientation to neural networks for cross-view geo-localization. In *Proceedings of the IEEE/CVF conference on computer vision and pattern recognition*, pp. 5624–5633, 2019.

Zhuang Liu, Hanzi Mao, Chao-Yuan Wu, Christoph Feichtenhofer, Trevor Darrell, and Saining Xie. A convnet for the 2020s. In *Proceedings of the IEEE/CVF conference on computer vision and pattern recognition*, pp. 11976–11986, 2022.

Tom Nowak, Alexander Große-Kreul, Marius Boshoff, and Bernd Kuhlenkötter. Enhancing mobile robot position estimation with machine learning methods using camera-based tracking. *Procedia CIRP*, 130:964–968, 2024.

OpenAI. Gpt-4 technical report. volume abs/2303.08774, 2023.

Krishna Regmi and Mubarak Shah. Bridging the domain gap for ground-to-aerial image matching. *2019 IEEE/CVF International Conference on Computer Vision (ICCV)*, pp. 470–479, 2019. URL <https://api.semanticscholar.org/CorpusID:131776514>.

Nils Reimers and Iryna Gurevych. Sentence-bert: Sentence embeddings using siamese bert-networks. *arXiv preprint arXiv:1908.10084*, 2019.

Supriya Sathyanarayana, Christoph Leuze, Brian Hargreaves, Bruce Daniel, Gordon Wetzstein, Amit Etkin, Mahendra T Bhati, and Jennifer A McNab. Comparison of head pose tracking methods for mixed-reality neuronavigation for transcranial magnetic stimulation. In *Medical imaging 2020: Image-guided procedures, robotic interventions, and modeling*, volume 11315, pp. 147–154. SPIE, 2020.

Jakub Semborski and Adam Idzkowski. A review on positioning techniques of mobile robots. *Robotic Systems and Applications*, 4(1):30–43, 2024.

Tianrui Shen, Yingmei Wei, Lai Kang, Shanshan Wan, and Yee-Hong Yang. Mccg: A convnext-based multiple-classifier method for cross-view geo-localization. *IEEE Transactions on Circuits and Systems for Video Technology*, 34(3):1456–1468, 2023.

Yujiao Shi, Liu Liu, Xin Yu, and Hongdong Li. Spatial-aware feature aggregation for image based cross-view geo-localization. *Advances in Neural Information Processing Systems*, 32, 2019.

Yujiao Shi, Xin Yu, Liu Liu, Tong Zhang, and Hongdong Li. Optimal feature transport for cross-view image geo-localization. In *Proceedings of the AAAI Conference on Artificial Intelligence*, volume 34, pp. 11990–11997, 2020.

Taro Suzuki, Yusuke Takahashi, and Yoshiharu Amano. Precise uav position and attitude estimation by multiple gnss receivers for 3d mapping. In *Proceedings of the 29th International Technical Meeting of the Satellite Division of The Institute of Navigation (ION GNSS+ 2016)*, pp. 1455–1464, 2016.

Volcengine. Doubao-1.5-thinking-vision-pro, 2025. URL <https://www.volcengine.com/docs/82379/1554521>.

Tingyu Wang, Zhedong Zheng, Yaoqi Sun, Chenggang Yan, Yi Yang, and Tat-Seng Chua. Multiple-environment self-adaptive network for aerial-view geo-localization. *Pattern Recognition*, 152:110363, 2024.

Weiyun Wang, Zhangwei Gao, Lixin Gu, Hengjun Pu, Long Cui, Xingguang Wei, Zhaoyang Liu, Linglin Jing, Shenglong Ye, Jie Shao, et al. Internvl3. 5: Advancing open-source multimodal models in versatility, reasoning, and efficiency. *arXiv preprint arXiv:2508.18265*, 2025.

Scott Workman, Richard Souvenir, and Nathan Jacobs. Wide-area image geolocalization with aerial reference imagery. In *Proceedings of the IEEE International Conference on Computer Vision*, pp. 3961–3969, 2015.

Qiong Wu, Panwang Xia, Lei Yu, Yi Liu, Mingtao Xiong, Liheng Zhong, Jingdong Chen, Ming Yang, Yongjun Zhang, and Yi Wan. Cross-view image set geo-localization. *ArXiv*, abs/2412.18852, 2024a.

Qiong Wu, Panwang Xia, Lei Yu, Yi Liu, Mingtao Xiong, Liheng Zhong, Jingdong Chen, Ming Yang, Yongjun Zhang, and Yi Wan. Cross-view image set geo-localization. *arXiv preprint arXiv:2412.18852*, 2024b.

Panwang Xia, Yi Wan, Zhi Zheng, Yongjun Zhang, and Jiwei Deng. Enhancing cross-view geo-localization with domain alignment and scene consistency. *IEEE Transactions on Circuits and Systems for Video Technology*, 2024a.

Panwang Xia, Yi Wan, Zhiwei Zheng, Yongjun Zhang, and Jiwei Deng. Enhancing cross-view geo-localization with domain alignment and scene consistency. *IEEE Transactions on Circuits and Systems for Video Technology*, 34:13271–13281, 2024b. URL <https://api.semanticscholar.org/CorpusID:272153723>.

Jinheng Xie, Weijia Mao, Zechen Bai, David Junhao Zhang, Weihao Wang, Kevin Qinghong Lin, Yuchao Gu, Zhijie Chen, Zhenheng Yang, and Mike Zheng Shou. Show-o: One single transformer to unify multimodal understanding and generation. *arXiv preprint arXiv:2408.12528*, 2024.

Jiaqi Xu, Zhou Chen, Jie Chen, Jingyan Zhou, and Xiaofei Du. A precise localization algorithm for unmanned aerial vehicles integrating visual-internal odometry and cartographer. *Journal of Measurements in Engineering*, 12(2):284–297, 2024.

Yuan Yao, Tianyu Yu, Ao Zhang, Chongyi Wang, Junbo Cui, Hongji Zhu, Tianchi Cai, Haoyu Li, Weilin Zhao, Zhihui He, et al. Minicpm-v: A gpt-4v level mllm on your phone. *arXiv preprint arXiv:2408.01800*, 2024.

Yiming Zhao, Xinming Huang, and Ziming Zhang. Deep lucas-kanade homography for multi-modal image alignment. *2021 IEEE/CVF Conference on Computer Vision and Pattern Recognition (CVPR)*, pp. 15945–15954, 2021. URL <https://api.semanticscholar.org/CorpusID:233387971>.

Zhedong Zheng, Yunchao Wei, and Yi Yang. University-1652: A multi-view multi-source benchmark for drone-based geo-localization. In *Proceedings of the 28th ACM international conference on Multimedia*, pp. 1395–1403, 2020.

Jinguo Zhu, Weiyun Wang, Zhe Chen, Zhaoyang Liu, Shenglong Ye, Lixin Gu, Yuchen Duan, Hao Tian, Weijie Su, Jie Shao, Zhangwei Gao, Erfei Cui, Yue Cao, Yangzhou Liu, Haomin Wang, Weiye Xu, Hao Li, Jiahao Wang, Han Lv, Dengnian Chen, Songze Li, Yinan He, Tan Jiang, Jiapeng Luo, Yi Wang, Cong He, Botian Shi, Xingcheng Zhang, Wenqi Shao, Junjun He, Ying Xiong, Wenwen Qu, Peng Sun, Penglong Jiao, Lijun Wu, Kai Zhang, Hui Deng, Jiaye Ge, Kaiming Chen, Limin Wang, Min Dou, Lewei Lu, Xizhou Zhu, Tong Lu, Dahua Lin, Yu Qiao, Jifeng Dai, and Wenhui Wang. Internvl3: Exploring advanced training and test-time recipes for open-source multimodal models. *ArXiv*, abs/2504.10479, 2025. URL <https://api.semanticscholar.org/CorpusID:277780955>.

Sijie Zhu, Taojiannan Yang, and Chen Chen. Vigor: Cross-view image geo-localization beyond one-to-one retrieval. In *Proceedings of the IEEE/CVF Conference on Computer Vision and Pattern Recognition*, pp. 3640–3649, 2021.

A APPENDIX

A.1 PSEUDOCODE FOR THE DDP LOSS COMPUTATION

We provide the pseudocode for DDP loss computation below.

Algorithm 1: Distributed InfoNCE Loss (DDP)

Input: Image features $\mathbf{f}_1, \mathbf{f}_2 \in \mathbb{R}^{B \times d}$, logit scale α , world size W , rank r
Output: Contrastive loss \mathcal{L} on rank r

- 1 Normalize features: $\mathbf{f}_1 \leftarrow \text{normalize}(\mathbf{f}_1)$, $\mathbf{f}_2 \leftarrow \text{normalize}(\mathbf{f}_2)$;
- 2 Gather features from all processes:

$$\{\mathbf{f}_1^{(w)}\}_{w=1}^W \leftarrow \text{AllGather}(\mathbf{f}_1), \quad \{\mathbf{f}_2^{(w)}\}_{w=1}^W \leftarrow \text{AllGather}(\mathbf{f}_2)$$

- 3 Concatenate features, excluding local rank duplicates:

$$\mathbf{F}_1 \leftarrow [\mathbf{f}_1] \cup \{\mathbf{f}_1^{(w)} \mid w \neq r\}, \quad \mathbf{F}_2 \leftarrow [\mathbf{f}_2] \cup \{\mathbf{f}_2^{(w)} \mid w \neq r\}$$

- 4 Compute logits:

$$\mathbf{Z}_1 = \alpha \cdot \mathbf{F}_1 \mathbf{F}_2^\top, \quad \mathbf{Z}_2 = \mathbf{Z}_1^\top$$

- 5 Construct global labels:

$$\mathbf{y} = [0, 1, \dots, N-1], \quad N = \text{rows}(\mathbf{Z}_1)$$

- 6 Compute loss:

$$\mathcal{L} = \frac{1}{2}(\text{CE}(\mathbf{Z}_1, \mathbf{y}) + \text{CE}(\mathbf{Z}_2, \mathbf{y}))$$

return \mathcal{L} ;

A.2 DETAILS OF HUMAN ANNOTATORS

In the Data Annotation stage, we hire 4 human experts in Remote Sensing, each holding at least a master’s degree. We pay them a labeling fee of \$20 per hour.

A.3 HYPER-PARAMETERS

A.3.1 GLEAM-C

Here we provide the training hyper-parameters of GLEAM-C using PE-Core-L14-336 ViT on the second training phase.

Parameter	Value
Model	PE-Core-L14-336
Epochs	40
Batch Size (Total)	300
Learning Rate	1e-4
Scheduler	Cosine
Warmup Epochs	1
Label Smoothing	0.1
Neighbour Select	64
Neighbour Range	128
Prob Rotate	0.75
Prob Flip	0.5

Table 7: Training hyper-parameters of GLEAM-C using PE-Core-L14-336.

A.3.2 GLEAM-X

Here we provide the hyper-parameters of training Qwen2.5-VL-3B-Instruct on GLEAM-X.

Parameter	Value
Learning Rate	5e-5
Batch Size (Total)	60
Epochs	1
Weight Decay	0.1
Warmup Ratio	0.05
Max Length	2048
Min/Max Pixels	256/1296
Gradient Checkpointing	True
Precision	BF16

Table 8: Hyper-parameters of training Qwen2.5-VL-3B-Instruct on GLEAM-X.

A.4 MORE DATA EXAMPLES OF GLEAM-X.

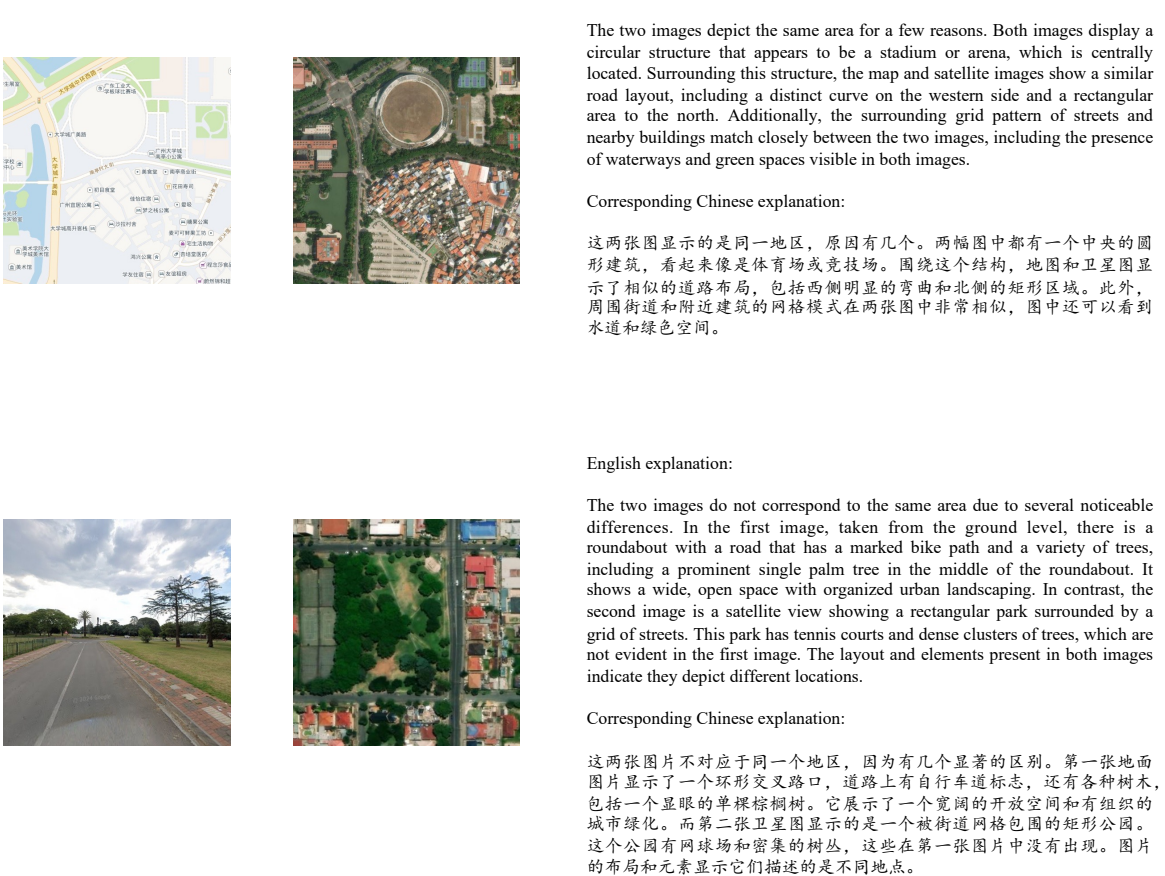


Figure 3: Street map and ground photograph samples.



English explanation:

The first image is a panoramic view from a street-level perspective, showing a street scene under an elevated train track structure. The recognizable feature is the steel structure supporting the train tracks above, with cars parked on the street below. The second image is a satellite view showing an urban area with an elevated track visible as a thin line crossing over a street. The satellite image clearly shows the elevated structure aligned with the street below, which matches the street structure and alignment shown in the panoramic view. The presence of buildings and the layout of the road network support the idea that both images represent the same location.

Corresponding Chinese explanation:

第一张图片是从街道层面的全景视角，展示了高架铁路轨道结构下的街景。可以辨认出的特征是上方的火车轨道支撑的钢结构，下面是街道上停放的汽车。第二张图片是卫星视图，显示一个城市区域，有一个明显的高架轨道如同一条细线横跨街道。卫星图像清楚地显示高架结构与下面的街道对齐，这与全景图中展示的街道结构和对齐方式一致。建筑物的存在和道路网络的布局支持了这两个图像代表同一位置的观点。



English explanation:

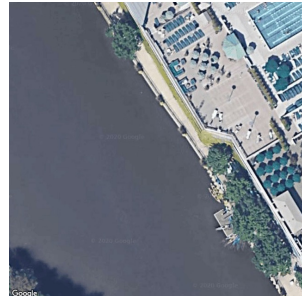
The two images do not correspond to the same area for several reasons. First, the architectural style of the buildings is different; the first image features a more modern structure with clear geometric lines and distinct surfaces, while the second image shows a complex of buildings with different layouts. Second, the surrounding environment is not similar: the first image has dense greenery and natural surroundings, whereas the second image has an organized path layout. Additionally, the second image shows more connections between buildings, indicating a different setting, possibly a campus or a similar complex.

Corresponding Chinese explanation:

这两张图片对应的区域不同，原因有几个。首先，建筑风格不同：第一张图中的建筑呈现出现代的风格，有明显的几何线条和表面，而第二张图中的建筑群布局不同。其次，周围环境不同：第一张图展示了密集的绿地和自然环境，而第二张图则有井然有序的小路布局。此外，第二张图片中的建筑物之间有更多的连接，表明这是一个不同的环境，可能是一个校园或类似的建筑群。

Figure 4: Panoramic view and UAV imagery samples.

A.5 MORE QUALITATIVE RESULTS ON GLEAM-X BENCHMARK

Ground-Truth

[[1]]
这两幅图像很可能对应同一地区，因为两者中都可见明显的特征。在全景图中，河流和周围的建筑物显示出一个独特的城市滨水区。卫星图像显示了一个有相邻建筑物和游泳池的河岸，这表明它也是一个城市河边位置。两幅图像中常见的相似结构，如高层建筑和沿河的树木、路径，都支持它们描绘的是同一地点的观点。

[[1]]
The two images likely correspond to the same area due to identifiable features visible in both. In the panoramic image, the river and surrounding buildings suggest a distinctive urban waterfront area. The satellite image shows a waterfront with adjacent buildings and a swimming pool, indicating it's also an urban riverside location. The presence of similar structures, like high-rise buildings and waterfront features, such as trees lining the river and pathways, is common in both images, supporting the idea that they depict the same location.

GPT-4o

[[1]]
这两张图片看起来对应同一个地区，主要理由如下：
1. **水体和建筑**：第一张全景图显示了一个城市河流的景观，周围有现代化的高楼建筑。卫星图也显示了一个水体周围有建筑的区域。整体都市和水体布局相似。
2. **环境特征**：全景图中可以看到河流和沿河绿化，卫星图中也明显有沿水体的绿地和路径。
3. **桥梁和建筑布局**：从全景图中可以看到桥梁的结构和建筑的分布，似乎与卫星图中建筑和道路的配置相吻合。
综合以上因素，两个图像展示的环境特征和建筑特点相似，很可能是同一个地区。

[[1]]
These two images appear to correspond to the same area, primarily for the following reasons:
1. **Water bodies and buildings**: The first panorama depicts a city river landscape surrounded by modern high-rise buildings. The satellite image also shows an area with buildings surrounding a water body. The overall urban and water body layout is similar.
2. **Environmental features**: The panorama reveals a river with riverside greenery, while the satellite image clearly shows green spaces and pathways along the water body.
3. **Bridge and Building Layout**: The panorama depicts bridge structures and building distributions that appear to align with the configuration of buildings and roads in the satellite image.
Considering these factors collectively, the environmental features and architectural characteristics displayed in both images are similar, strongly suggesting they depict the same area.

Qwen2.5-VL-3B-Instruct

[[0]]
解释：
这两张图片虽然都展示了河流和城市景观，但它们对应的是不同的地区。第一张图片显示的是一个城市河岸，有建筑物、树木和船只，背景是蓝天。第二张图片显示的是一个湖泊或河流的卫星图像，有码头、船只和树木，但没有建筑物。因此，这两张图片对应的是不同的地区。

[[0]]
Although both images depict rivers and urban landscapes, they correspond to different regions. The first image shows a city riverbank with buildings, trees, and boats against a blue sky backdrop. The second image presents a satellite view of a lake or river featuring docks, boats, and trees, but no buildings. Therefore, these two images correspond to distinct locations.

Qwen2.5-VL-3B-Instruct + label only

[[1]]

Qwen2.5-VL-3B-Instruct + GPT-4o

[[1]]
这两张图片对应同一地区，因为它们都显示了一个滨水区域，有明显的特征。在全景图中，可以看到一条河流或运河，河岸边有木制的护岸，旁边有建筑物和树木。卫星图显示了类似的滨水区域，有水体、岸边的树木和建筑物。卫星图中建筑物的形状和布局与全景图中看到的建筑相匹配。此外，全景图中可见的桥梁结构与卫星图中水边的结构相对应。这些共同的元素确认了两张图片是同一地点的不同视角。

[[1]]
These two images correspond to the same area, as both depict a distinct waterfront region with recognizable features. The panoramic image shows a river or canal with wooden revetments along the banks, flanked by buildings and trees. The satellite image reveals a similar waterfront area featuring a body of water, trees along the shoreline, and structures. The shapes and layout of the buildings in the satellite image match those visible in the panoramic view. Additionally, the bridge structure discernible in the panoramic view corresponds to the structure near the water's edge in the satellite image. These shared elements confirm that the two images represent different perspectives of the same location.

Figure 5: Sample on the VIGOR test set (Chinese scenario). The gray English text is a direct translation of the Chinese response.



Ground-Truth

[[0]]
 The two images do not correspond to the same area for several reasons. In the first image, there is a building with a modern architectural style, characterized by flat roofs and large panes of reflective glass, typical of an office or technology park. It is surrounded by parking lots and green space, including a soccer field. In contrast, the second image shows buildings with classic architecture, featuring more traditional designs with pointed roofs and a courtyard area, which are often associated with historical institutions such as universities or government buildings. Additionally, the layout of pathways and the arrangement of the surrounding greenery differ significantly between the two images.

Doubao-1.5-Thinking-Vision-Pro

[[0]]
 Explanation: To determine if the two images correspond to the same area, we analyze key features: \n1. **Building Architecture and Roof**: The first image shows a building with a dark - colored roof (likely solar panels or dark roofing material) and extensive glass - walled facades. The second image features a building with a light - colored, flat roof and a large rectangular skylight. These architectural differences are significant. \n2. **Surrounding Landscape and Layout**: The first image has a soccer field with visible goalposts adjacent to the building, along with parking lots and multi - lane roads. The second image shows a different field layout (no visible goalposts matching the first image's field) and a distinct road and sidewalk arrangement. \n3. **Contextual Elements**: The overall environment, including tree placement, road patterns, and the relationship between buildings and open spaces, does not match between the two images. \n\nDue to these substantial differences in building design, landscape features, and spatial context, the two images do not correspond to the same area.

Qwen2.5-VL-3B-Instruct

[[0]]
 Explanation:
 The two images provided do not correspond to the same area. The first image is an aerial view of a building with a flat roof and a parking lot in the background. The second image is a satellite view of a different area, showing a building with a sloped roof and a grassy area in the foreground. The buildings and their surroundings in the two images are distinct, indicating that they are not the same location.

Qwen2.5-VL-3B-Instruct + label only

[[0]]

Qwen2.5-VL-3B-Instruct + Doubao-1.5-Thinking-Vision-Pro

[[0]]
 The first image shows a modern building with a large glass facade, solar panels on the roof, and a sports field adjacent to it, along with a parking lot. The second image depicts a more traditional, possibly institutional or historical building complex with multiple connected structures, courtyards, and a different layout of green spaces and pathways. The architectural styles, building layouts, and surrounding features (like the sports field vs. the courtyard) are distinct, indicating different areas.

Figure 6: Sample on the University-1652 test set (English scenario).